ENSO-induced latitudinal variation of the subtropical jet modulates extreme winter precipitation over the Western Himalaya

It is advisable to refer to the publisher's version if you intend to cite from the work. See Guidance on citing.

To link to this article DOI: http://dx.doi.org/10.1007/s00376-024-4057-2

www.reading.ac.uk/centaur

• Original Paper •

ENSO-induced Latitudinal Variation of the Subtropical Jet Modulates Extreme Winter Precipitation over the Western Himalaya

Priya BHARATI[1], Pranab DEB[1], Kieran M. R. HUNT[2,3], Andrew ORR[*4], and Mihir Kumar DASH[1]

[1]*Centre for Ocean, River, Atmosphere and Land Sciences (CORAL), Indian Institute of Technology Kharagpur, Kharagpur 721302, India*

[2]*Department of Meteorology, University of Reading, Reading, RG6 6ET, UK*

[3]*National Centre for Atmospheric Science, University of Reading, RG6 6ET, UK*

[4]*British Antarctic Survey, Cambridge, CB3 0ET, UK*

ABSTRACT

In this study, we investigate the complex relationship between western disturbances (WDs), the El Niño–Southern Oscillation (ENSO), and extreme precipitation events (EPEs) in the western Himalaya (WH) during the extended winter season (November–March). WDs west of WH coincide with 97% of recorded EPEs, contributing substantially (32% in winter, 11% annually) to total precipitation within WH. WDs are 6% less frequent and 4% more intense during El Niño than La Niña to the west of WH. During El Niño (compared to La Niña) years, WDs co-occurring with EPEs are significantly more intense and associated with 17% higher moisture transport over "WH box" (the selected region where most of the winter precipitation over WH occurs). This results in twice the EPE frequency during El Niño periods than La Niña periods. A substantial southward shift (~180 km) of the subtropical jet (STJ) axis during El Niño brings WD tracks further south towards their primary moisture sources, especially the Arabian Sea. We have shown that WDs that are both more intense and pass to the south of their typical latitudes have higher levels of vertically integrated moisture flux (VIMF) within them. VIMF convergence in the most intense pentile of WDs is 5.7 times higher than in the weakest, and is 3.4 times higher in the second lowest latitude pentile than in the highest. Overall, this study demonstrates a direct link between changes in the latitudinal position and intensity of WDs associated with the winter STJ, and moisture convergence, which leads to the occurrence of EPEs over WH during ENSO phases.

Key words: western Himalaya, extreme precipitation, western disturbances, ENSO, moisture flux, winter

Article Highlights:

• During El Niño, there are more intense western disturbances (WDs) south of their typical latitudes.

• These WDs transport higher moisture and bring more frequent winter precipitation extremes over the western Himalaya.

---

1. Introduction:

The western Himalaya (WH) are highly susceptible to extreme precipitation events (EPEs) (e.g., Nandargi and Dhar, 2011; Thayyen et al., 2013; Dimri et al., 2017). These events often occur as heavy snowfall (Hewitt, 2011; Dahri et al., 2018; Pritchard, 2021), which contributes to the regional snowpack and glaciers (Anders et al., 2006; Tahir et al., 2011; Bolch et al., 2012; Ridley et al., 2013; Cannon et al., 2016). Subsequent melting of these reserves during spring serves as a major source of downstream river flow and relief from drought to dense populations that are particularly vulnerable to water stress (Singh et al., 2011; Pritchard, 2019; Orr et al., 2022). EPEs can also trigger natural hazards such as landslides, snow avalanches and floods (Thayyen et al., 2013; Dimri et al., 2017; Hunt and Dimri, 2021), which pose threats to lives, infrastructure, agriculture, and the overall socioeconomic wellbeing of the communities living in the region (Orr et al., 2022).

Synoptic-scale winter storms embedded in the westerly winds associated with the subtropical jet (STJ), which are referred to as westerly disturbances (WDs), are responsible for most of the EPEs over WH (Cannon et al., 2015; Dimri et al., 2015). These are strongest when the winds associated with the WDs are oriented perpendicular to the steep terrain

---

* Corresponding author: Andrew ORR
  Email: anmcr@bas.ac.uk

that characterizes WH (Hunt et al., 2018b; Baudouin et al., 2020a, 2021), and are most common from December to March when the STJ is at its lowest latitude (Schiemann et al., 2009). Key characteristics of the STJ (e.g., its shear, waviness, and maximum wind speed) all influence the propagation of WDs (Barlow et al., 2005). During the months of December to March, WDs are dynamically more intense with deeper troughs when the STJ reaches its maximum strength, and this intensification is characterized by increased intensity of WDs, rather than frequency (Cannon et al., 2016). The WDs typically move eastwards across Northwest India with a frequency of around five or six events per year (Cannon et al., 2016; Hunt et al., 2018a), while during winter, WDs are estimated to occur at a frequency of approximately four to seven per month (Chattopadhyay, 1970; Mohanty et al., 1998; Dimri, 2006; Hunt et al., 2018a; Midhuna et al., 2020). Cannon et al. (2017) also stated that WDs remain active in the range of two to seven days, so it is crucial to investigate them at the daily timescale in order to explore their impact on EPEs. The moisture required for WD precipitation largely originates from the Arabian Sea (Barlow et al., 2005; Kar and Rana, 2014; Jeelani et al., 2018; Lone et al., 2020).

Remote forcing from El Niño–Southern Oscillation (ENSO) events is known to influence the frequency of winter EPEs over WH, with the number of events increasing during El Niño periods compared to neutral or La Niña periods (Syed et al., 2006; Cannon et al., 2017; Kamil et al., 2019). ENSO-driven shifts in the STJ, particularly during El Niño, also induce latitudinal variations in WDs (Hoell et al., 2014, 2018; Dimri et al., 2015; Hu et al., 2018; Hunt et al., 2018a; Ahmed et al., 2020). For example, El Niño events prompt a southward shift of the STJ axis and associated WD tracks over the Indian subcontinent due to anomalous cyclonic circulation caused by cooling near the Indo-Pacific warm pool

and adjacent regions (Yadav et al., 2009, 2010a, 2010b; Dimri, 2013); while conversely, during La Niña events, the STJ and associated WD tracks shift northwards (Yadav et al., 2013; Cannon et al., 2017; Hu et al., 2018). During El Niño, there is a strong barotropic Rossby wave response, seen in the upper-level geopotential height over high-altitude Asia and WH due to diabatic heating in the tropics, which leads to an intensified STJ and the deepened trough (Syed et al., 2006; Hoell et al., 2012; Cannon et al., 2015, 2017). Additionally, studies have highlighted the significant role of the circumglobal teleconnection pattern in driving the wintertime extreme precipitation over adjacent regions of WH such as the Tibetan Plateau (Huang et al., 2018; Qiu et al., 2019).

However, considerable uncertainty still exists on how (1) the changes in EPEs during different ENSO phases are linked to changes in WDs, and (2) the latitudinal shifts in WD tracks during different ENSO phases affect moisture convergence across WH, and hence EPEs. These represent significant research gaps that this study addresses by using a combination of ERA5 atmospheric reanalysis data (Hersbach et al., 2020) and a catalogue of the tracks of WDs that can influence the WH region.

2.   Data and methods

A region encompassing 27°–37°N and 67°–77°E (hereafter referred to as "WH box" and depicted by the blue rectangle in Fig. 1) is selected where most of the winter precipitation over WH occurs. Moreover, winter precipitation within WH box has been reported to be strongly modulated by ENSO. EPEs within WH box, during an extended winter period from November to March (NDJFM) from 1979 to 2020, are identified as events where daily precipitation amounts from ERA5 reanalysis exceed the 95th percentile of the baseline
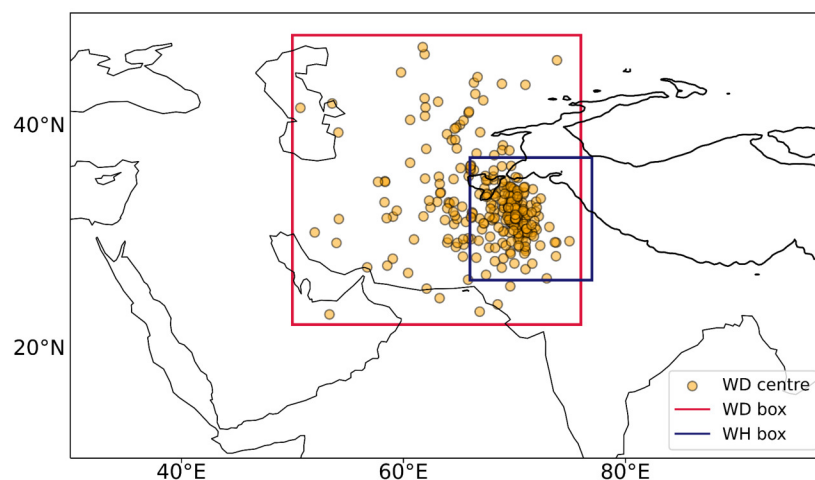

Fig. 1. Map showing the locations of the centers (orange-filled circles) of the 308 WDs within WD box (22°–47°N, 50°–77°E; red rectangle) that occurred contemporaneously with EPEs within WH box (27°–37°N, 67°–77°E; blue rectangle) during an extended winter period from November to March from 1979 to 2020. The thick black line denotes the 3000 m surface elevation contour.

(Syed et al., 2006; Yadav et al., 2009, 2010a, 2010b; Cannon et al., 2017; Kamil et al., 2019). Additionally, we found that the EPEs within WH box are associated with WDs that pass through a region encompassing 22°–47°N and 50°–77°E (hereafter referred to as "WD box" and depicted by the red rectangle in Fig. 1).

Furthermore, WDs within WD box during NDJFM from 1979 to 2020 are identified using a WD track catalogue described in Hunt et al. (2018a) and Sharma et al. (2022), which is based on ERA5 reanalysis data that are spectrally truncated to T42 to remove noise and small-scale structures. The tracking algorithm detects WDs by identifying upper-tropospheric regions of positive relative vorticity averaged between 450 and 300 hPa, with the locations of candidate WDs identified as centroids of these regions. The candidate WDs are then further refined by only accepting those (1) whose locations are linked through time to form tracks that generally follow the westerly steering winds associated with the STJ, (2) that persist for at least 48 hours, and (3) pass through North India (22°–42.5°N, 50°–77°E).

The daily geopotential height at 350 hPa from ERA5 is used to investigate the circulation associated with WDs and EPEs, while the intensity of a WD is defined as the daily 350 hPa relative vorticity at the centre of the WD. Daily zonal and meridional components of vertically integrated moisture flux (VIMF) from ERA5 are used to investigate the moisture transport associated with WDs and EPEs. The net moisture accumulation within WH box is also determined by (1) computing the average VIMF in the zonal direction along the easterly and westerly sides of WH box and the average VIMF in the meridional direction along the southerly and northerly sides of the box, and multiplying them by the respective lengths of the sides of the box, and (2) summing the differences between the zonal components (i.e., westerly minus easterly) and meridional components (northerly minus southerly), which are then divided by the area of the box. The monthly 200 hPa zonal wind speed from ERA5 is used to calculate the STJ axis location. This is defined as the latitude of its local maximum (greater than a threshold of 30 m s⁻¹), following Schiemann et al. (2009) and Hunt and Zaz (2023). These ERA5 fields are retrieved at a horizontal resolution of $0.25° × 0.25°$.

Finally, the changes in EPEs and WDs during different ENSO phases are examined by calculating the composite differences between El Niño and La Niña events. The Niño-3.4 monthly index from the National Oceanic and Atmospheric Administration's Climate Prediction Center is used to identify the phase of ENSO events during NDJFM from 1979 to 2020, with El Niño (La Niña) events corresponding to average sea surface temperature anomalies across the equatorial Pacific that are over one standard deviation above (below) average. This identified six El Niño events (1983, 1987, 1992, 1998, 2010, 2016) and six La Niña events (1985, 1989, 1999, 2000, 2008, 2011) from 1979 to 2020. Note that NDJFM is January-based, i.e., NDJFM 1983 refers to the boreal winter of 1982/83. Differences in the composites

are tested at the 95% confidence level using Welch's *t*-test.

3. Results

Based on the WD track catalogue, the total number of days over NDJFM from 1979 to 2020 that are associated with the center of a WD occurring within WD box was 5506. Based on ERA5 data, 308 of these days with WDs occurring within WD box are also associated with the contemporaneous occurrence of an EPE within WH box, with the majority of these WDs concentrated over the western part of WH box (Fig. 1). These collectively account for 97% of the 318 EPEs recorded within WH box for this period, as well as around 32% of the total winter precipitation and 11% of the total annual precipitation within WH box.

Figure 2a shows that the days in which WDs occurred within WD box are associated with an anomalous cyclonic system situated over the western part of WH box, with negative height anomalies at 350 hPa of up to −9 m. This anomalous cyclone is associated with enhanced northeasterly moisture transport over the western side of WD box, as well as enhanced westerly and southwesterly moisture transport over its southern side, with VIMF anomalies reaching 8 kg m⁻¹ s⁻¹. However, the VIMF anomalies are relatively low in WH box, with the exception of the southeast corner of the box. By contrast, the subset of events with WDs occurring with the contemporaneous occurrence of an EPE are associated with a much deeper anomalous cyclonic structure situated just west of WH box, with negative height anomalies at 350 hPa of up to −100 m associated with the strongest class of WDs (Fig. 2b). This is associated with enhanced westerly and southwesterly moisture transport over the southern side of the WD box from the Arabian Peninsula and Arabian Sea towards WH box, with VIMF anomalies reaching 150 kg m⁻¹ s⁻¹ over the eastern side of WH box.

Out of the 5506 days that WDs occurred within WD box over NDJFM from 1979 to 2020, 765 (13.8%) of them happened during the six El Niño periods, while 795 (14%) of them happened during the six La Niña periods during this time interval. Moreover, out of the 308 days that EPEs occurred contemporaneously with WDs from 1979 to 2020, 51 (16%) of them occurred during El Niño periods, while 26 (8%) occurred during La Niña periods. The average frequency and intensity of the EPEs that occurred contemporaneously with WDs are 8.5 per season and 9.4 mm d⁻¹ during El Niño events, and 4.3 per season and 8.5 mm d⁻¹ for La Niña events. This increase (doubling) of the frequency of EPEs occurring contemporaneously with WDs is consistent with previous studies showing that the number of EPEs over WH increases during El Niño periods compared to La Niña periods (Syed et al., 2006; Cannon et al., 2017; Kamil et al., 2019). Analysis of the net moisture accumulation within WH box for the EPEs occurring contemporaneously with WDs also shows a value of 6.6 × 10⁻⁵ kg m⁻² s⁻¹ during El Niño periods compared to 5.6 × 10⁻⁵ kg m⁻² s⁻¹ during La Niña periods. This net moisture accumulation is around
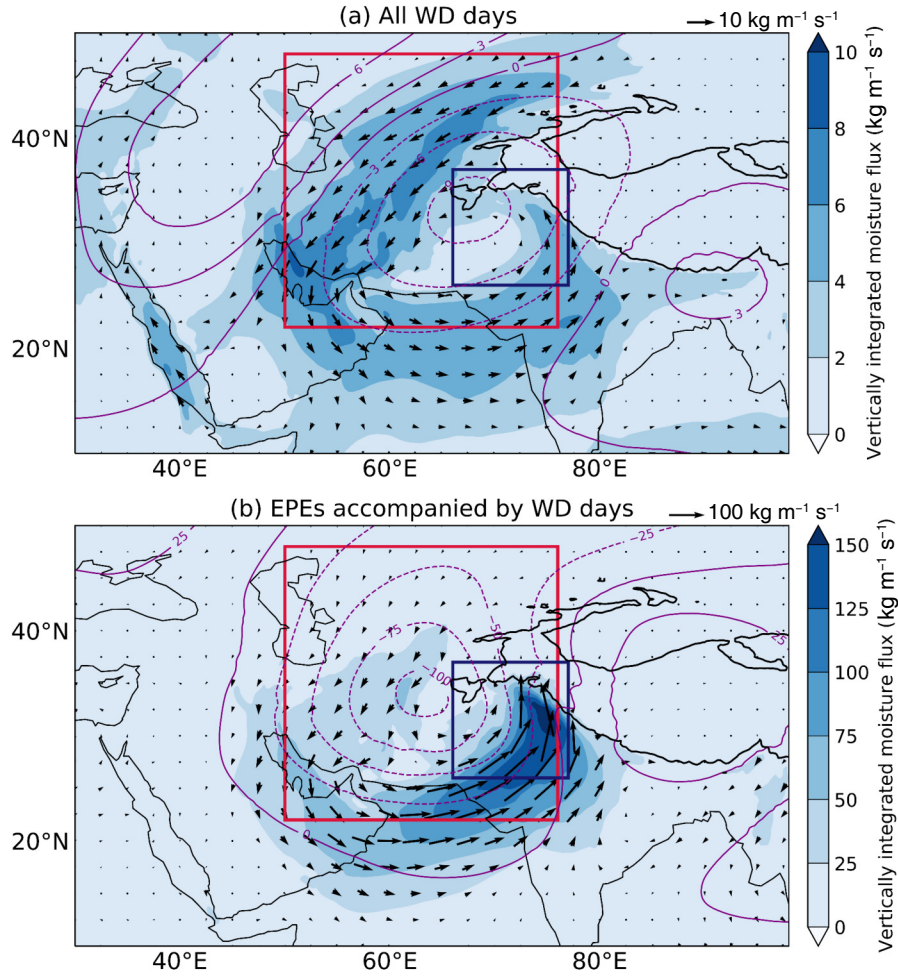
Fig. 2. Maps showing the daily average anomalies of the magnitude of VIMF (colours), VIMF (vectors; kg m^{-1} s^{-1}), and geopotential height at 350 hPa (contours; m) during an extended winter period from November to March from 1979 to 2020 for (a) the 5506 days that WDs occurred in WD box, and (b) the 308 days that EPEs in WH box coincided with the occurrence of WDs in WD box. The two boxes (WD and WH) are shown as red and blue rectangles, respectively. In (a), the reference VIMF vector, maximum VIMF magnitude, and 350 hPa contour interval are 10 kg m^{-1} s^{-1}, 10 kg m^{-1} s^{-1}, and 3 m, respectively; while in (b), they are 100 kg m^{-1} s^{-1}, 150 kg m^{-1} s^{-1}, and 25 m.

17% higher over WH box during El Niño periods than during La Niña periods.

To investigate how the different ENSO phases are linked to changes in WDs, we show composites of differences between the 765 days when WDs occurred during El Niño periods and the 795 days when the WDs occurred during La Niña periods (Fig. 3a). This shows a deepening and westward shift of the anomalous cyclonic system seen in Fig. 2a, with negative differences in geopotential height at 350 hPa of up to −20 m to the west of WD box. This results in a reduction in the northeasterly moisture transport over the western side of WD box, with the VIMF being up to 10 kg m^{-1} s^{-1} less over this region during El Niño periods compared to La Niña periods. In contrast, this also results in a small increase in the westerly and southwesterly moisture transport over the southern side of WD box, with the VIMF being up to 5 kg m^{-1} s^{-1} greater over this region during El Niño periods

compared to La Niña periods. This is associated with a band of enhanced anomalous VIMF that stretches from eastern Africa, across the Arabian Peninsula and Arabian Sea, towards WH box. This results in substantial VIMF convergence of about 2.5×10^{-5} kg m^{-2} s^{-1} over WH for WD days that occur during El Niño periods compared to La Niña periods. The higher VIMF convergence over WH on WD days that occur during El Niño compared to La Niña is consistent with the asymmetric responses of El Niño and La Niña on the upper geopotential anomalies in WD box and the VIMF pattern across the Indian Ocean and Arabian Peninsula [Fig. S1, in the electronic supplementary material (ESM)].

To further investigate how these changes in EPEs during different ENSO phases are linked to changes in WDs, Fig. 3b shows a composite of the differences between the 51 days during El Niño periods and the 26 days during La Niña periods in which EPEs occurred contemporaneously with
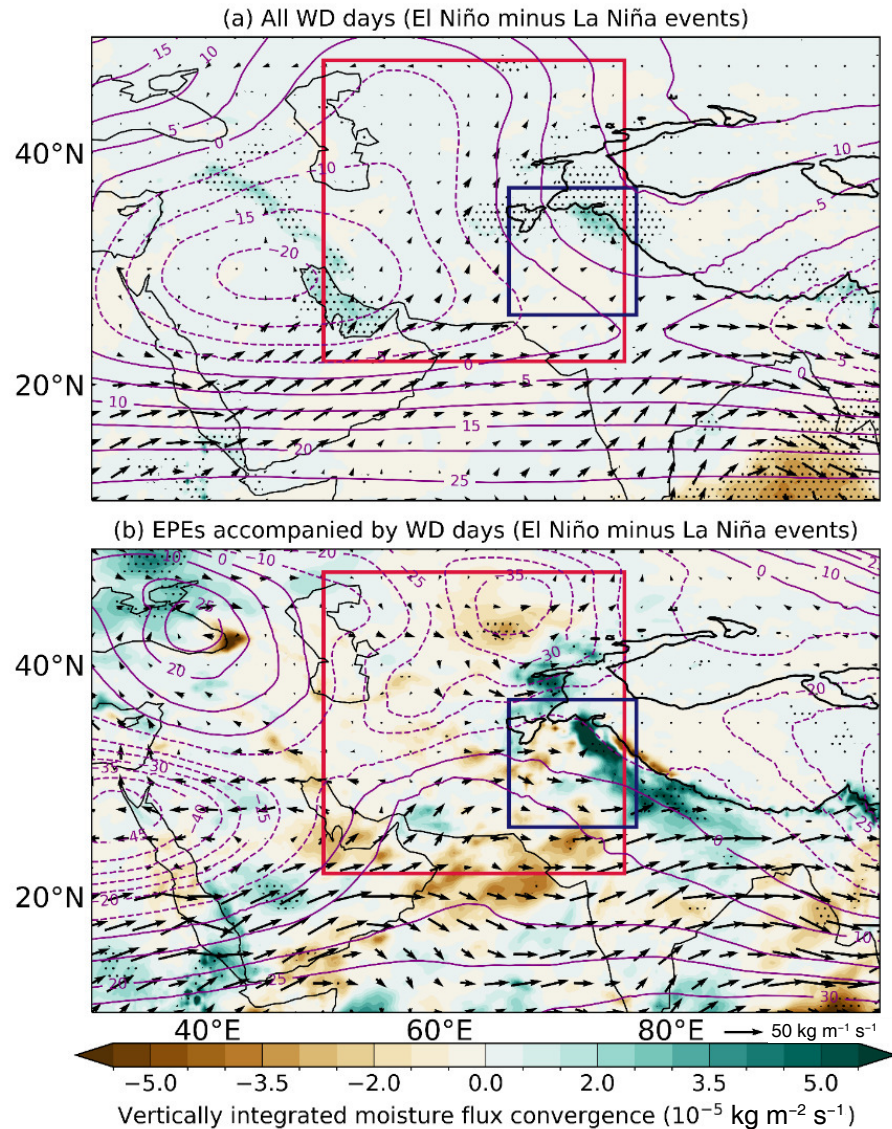
Fig. 3. Maps showing the composite differences of VIMF convergence (colours; 10^{-5} kg m^{-2} s^{-1}), VIMF (vectors; kg m^{-1} s^{-1}), and geopotential height at 350 hPa (contours; m) between El Niño and La Niña events during an extended winter period from November to March from 1979 to 2020 for (a) the days that WDs occurred in WD box (765 for El Niño, 795 for La Niña), and (b) the days that EPEs in WH box coincided with the occurrence of WDs in WD box (51 for El Niño, 26 for La Niña). Areas with stippling indicate where the differences are significant at a 95% confidence level. The two boxes (WD and WH) are shown as red and blue rectangles, respectively.

WDs. This difference shows a deeper anomalous cyclonic system in WD box, with a difference in geopotential height at 350 hPa of up to −45 m southwestward of the west of WD box during El Niño periods. A marked increase is observed in southwesterly moisture transport from the Arabian Peninsula and Arabian Sea towards WH box, with VIMF anomalies reaching 40 kg m^{-1} s^{-1} over the southern side of WD box and up to 20 kg m^{-1} s^{-1} over the southern and central sections of WH box, i.e., consistent with enhanced moisture convergence during El Niño periods, and an increase in the frequency of EPEs. The robust easterly movement of moisture across the equatorial Indian Ocean (not shown), along with westerly

movement of moisture from the Arabian Peninsula and Arabian Sea towards WH box, leads to the strong moisture convergence with VIMF convergence of up to 5×10^{-5} kg m^{-2} s^{-1} over WH for EPEs occurring simultaneously with WDs during El Niño periods compared to La Niña periods. A significant increase in VIMF convergence (Fig 3b) over WH is caused by a stronger and wider band of moist westerlies impacting the region during El Niño compared to La Niña (Fig. S1 in the ESM). Conversely, a weaker cyclonic circulation evident at the 350 hPa level within WD box, moving towards an area with a deepened anticyclonic circulation (a shortwave pattern with less zonal structure) lowered the oro-

graphic precipitation over WH during La Niña (Fig. S1 in the ESM).

Background changes in the large-scale upper-level atmospheric circulation, such as modifications in the winter jet stream induced by contrasting ENSO phases, have a significant impact on lower-level circulation patterns and hence moisture availability in the region, creating diverse atmospheric conditions that individual WDs encounter. Therefore, understanding the mean changes in the background atmosphere is key in comprehending the occurrences of individual EPEs over WH. In Fig. 4, the mean position of the STJ axis is depicted during boreal winter for both El Niño and La Niña periods. During El Niño, the STJ axis undergoes a meridional shift of approximately 180 km southward, relative to the La Niña average, as it traverses WD box. Concurrent with this, the composite difference in winter zonal wind speed at 200 hPa between El Niño and La Niña periods reveals an intensification of upper-level westerlies in the southern part of WD box. In contrast, during La Niña winters, the STJ exhibits a poleward shift that directs WD tracks away from the Arabian Sea, consequently leading to reduced moisture transport towards WH.

Changes in the STJ have a substantial impact on the frequency and intensity of WDs, thus directly shaping the seasonal precipitation patterns across WH. Figure 5 examines the changes in the frequency and intensity of WDs in WD box during different ENSO phases. In boreal winter during 1979 to 2020, the average distribution of WDs within WD box shows a frequency range of one to three occurrences per season per $(100 \text{ km})^2$, with the highest frequency concentrated in WH box (Fig. 5a). Overall, the average WD frequency over WD box is around 6% lower during El Niño years compared to La Niña years. During El Niño periods (relative to La Niña periods), the frequency of WDs decreases

by around 9% [by around 0.5 occurrences per season per $(100 \text{ km})^2$] over the area encompassing WH box and the northern part of WD box, but increases by around 5% [by around 0.3 occurrences per season per $(100 \text{ km})^2$] over the southwestern (or equatorward) part of WD box. The mean value of WD intensity is approximately $10 \times 10^{-5} \text{ s}^{-1}$ across WD box, with peak value reaching up to $14 \times 10^{-5} \text{ s}^{-1}$ in the WH area and the northern part of WD box (Fig. 5c). An equatorward shift is also apparent in the intensity of the WDs, which decreases over the northern sectors of WD box by around 2% (up to $0.3 \times 10^{-5} \text{ s}^{-1}$) but increases by up to 5% (by $0.5 \times 10^{-5} \text{ s}^{-1}$) over the southern sectors during El Niño periods compared to La Niña periods. Overall, WD intensity is 4% higher over WD box during El Niño periods compared to La Niña periods. This equatorward shift of the WD tracks during El Niño periods is consistent with the southward displacement of the STJ (which they are embedded in) within WD box.

We hypothesize, in accordance with Baudouin et al. (2021), that the closer proximity of southward-shifted WD tracks to the Arabian Sea results in a more abundant moisture supply, which plays a pivotal role in intensifying the regional precipitation during extreme El Niño periods. We test this directly by stratifying WD-centered composites of WD moisture flux and moisture flux convergence by WD intensity and latitude (Fig. 6). Here, we take all WDs between 60°E and 80°E and compute the pentiles of their latitude and intensity (for which we use the 350 hPa T63 relative vorticity). This stratified composite provides strong evidence that VIMF is larger in WDs that are both more intense and pass south of their typical latitudes, both of which work to increase their moisture supply. Intensity is the stronger driver; the VIMF convergence composite maxima for each intensity pentile are 2.1, 3.2, 3.9, 6.8 and $12.1 \times 10^{-5} \text{ kg m}^{-2} \text{ s}^{-1}$,
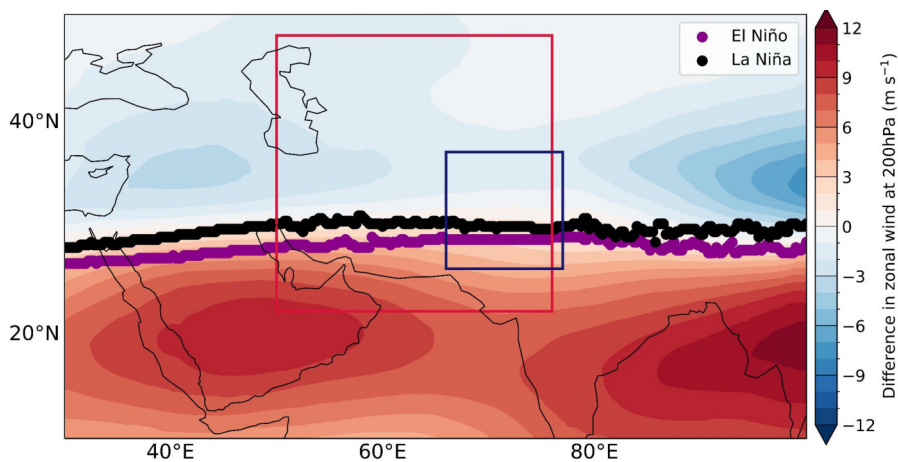

Fig. 4. Map showing the composite difference of monthly zonal wind speed at 200 hPa between El Niño and La Niña events during an extended winter period from November to March from 1979 to 2020 (shading; m s^{-1}). The mean positions of the subtropical westerly jet axis for these El Niño and La Niña events are also shown, as magenta and black circles, respectively. The two boxes (WD and WH) are shown as red and blue rectangles, respectively.
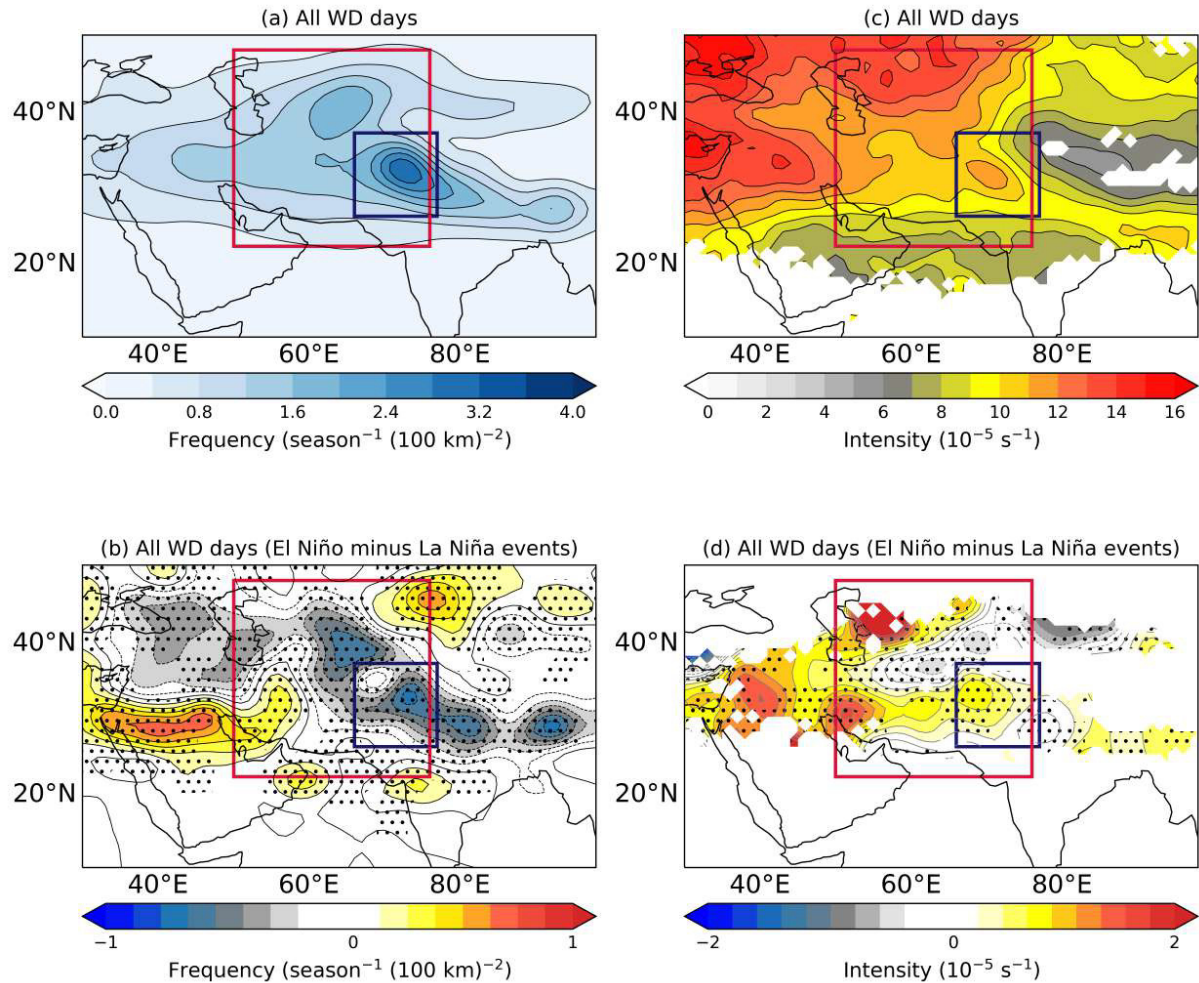
Fig. 5. Maps showing the climatological (a) frequency [per season per (100 km)²] and (c) intensity (×10⁻⁵ s⁻¹) of WDs during an extended winter period from November to March from 1979 to 2020. Composite difference of (b) frequency and (d) intensity of WDs between El Niño and La Niña years during NDJFM. Stippling in (b) and (d) indicate where the differences are significant at a 95% confidence level. The two boxes (WD and WH) are shown as red and green rectangles, respectively.

respectively. For latitude (going from the southernmost to northernmost pentile), the VIMF convergence composite maxima are 4.7, 8.3, 7.6, 5.2 and 2.5×10^{-5} kg m⁻² s⁻¹, respectively. If we exclude the bottom pentile of latitude (here, below 26.5°N), where WDs are too far away from the orography of the WH for much convergence to occur, then the effect of going from the highest latitude pentile to the lowest latitude pentile increases the average VIMF convergence maximum by a factor of 3.4. Going from the lowest intensity pentile to the highest conversely increases the average VIMF convergence maximum by a factor of 5.7. Crucially, these effects combine, meaning that to achieve a very high VIMF convergence, a WD needs both a high intensity and a low latitude. One caveat, however, is that WDs that are too far south (here, below 26.5°N) are too far away from the orography of WH, and so even though they are associated with large moisture flux, they have quite weak convergence.

4. Conclusions

Our study, spanning 1979 to 2020, examines the intricate relationship between WDs, ENSO, and EPEs in the WH region during the extended winter season (NDJFM). The WDs occurring within a specified area to the west of the WH region are contemporaneous with 97% of recorded EPEs and contribute significantly (32% in winter, 11% annually) to total precipitation within the WH region. Analysis of these events revealed that the WDs co-occurring with EPEs showed a deeper and westward-shifted cyclonic system, contributing to increased moisture transport towards WH box from the Arabian Sea.

In this study, we quantify the influence of distinct ENSO phases on the co-occurrence of EPEs with WDs over WH during NDJFM. Our findings indicate a doubling of the frequency and an approximate 11% rise in the intensity of EPEs during El Niño periods compared to La Niña, which aligns with existing research (Cannon et al., 2017). Examin-
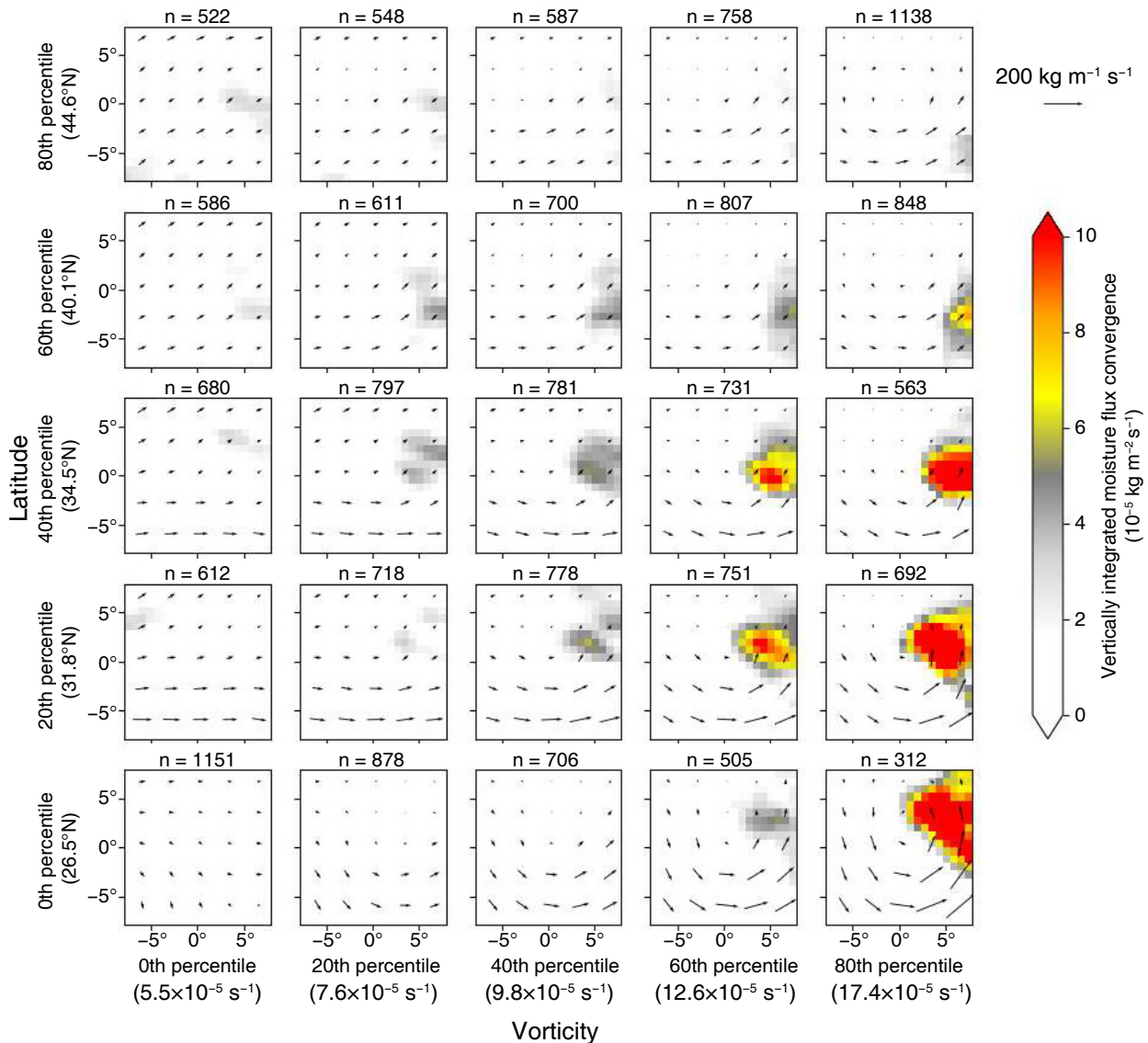
Fig. 6. System-centered average of VIMF (vectors; kg m^{-1} s^{-1}) and VIMF convergence (colours; 10^{-5} kg m^{-2} s^{-1}) for all WDs passing between 60°E and 80°E from November to March during 1979–2020. The composite is split into pentiles of latitude and intensity (measured using 350 hPa vorticity at the WD centre), with the labelled values indicating the upper bound of the pentiles that, e.g., the bottom-right panel shows the composite for WDs in the bottom pentile for latitude (having a centre south of 26.5°N) and top pentile of intensity (having 350 hPa relative vorticity between 12.6 and 17.4 × 10^{-5} s^{-1}). Each composite has longitude (relative to the system centre) on the *x*-axis and latitude (relative to the system centre) on the *y*-axis in the subplots.

ing the atmospheric circulation linked to EPEs during the contrasting ENSO phases revealed that the cyclonic circulation associated with WDs was more intense and shifted southward during El Niño phases. This shift greatly boosts southwesterly transport towards WH box, leading to an approximate 17% rise in total moisture accumulation over WH. These differences in moisture buildup and transport during ENSO phases highlight the influence of background atmospheric changes, particularly those of the STJ, with a substantial shift (by around 180 km) in its axis during El Niño periods (relative to La Niña periods), on extreme precipitation over WH. The southward shift in the STJ axis leads to a southward shift of WD tracks embedded within the jet. This has crucial

consequences for moisture supply and convergence over WH associated with WDs.

Our analysis also establishes a direct link between a southward shift in WD tracks, increasing proximity to the Arabian Sea, and heightened moisture supply, which in turn substantially impacts regional extreme precipitation during El Niño events. In summary, our study demonstrates that ENSO phases strongly control low-level circulation and moisture conditions, altering the background atmosphere, which subsequently affect WD behavior and the spatiotemporal dynamics of EPEs in WH during winter. The difference in winter precipitation over WH on WD days during ENSO phases arises due to asymmetric changes in moisture transport

across the Indian Ocean and Arabian Peninsula and upper-atmospheric geopotential anomalies in WD box, which are primarily a result of asymmetric responses to El Niño and La Niña (Chakraborty and Singhai, 2021). However, the co-occurrence of EPEs with WDs does not reveal any asymmetric response to ENSO phases.

It is important to acknowledge potential biases in gridded precipitation data over WH due to the limited number of in situ measurements and the complex topography of the area, which may affect the reliability of EPE statistics. However, recent research has shown that the daily precipitation dataset from the ERA5 reanalysis exhibits reasonable skill in capturing the spatial and temporal distribution of winter precipitation in the WH region when compared to gauge-based records and other reanalysis products (Baudouin et al., 2020b; Dahri et al., 2021; Singh et al., 2021; Bhattacharyya et al., 2022). Continuing our research into the drivers of winter precipitation across WH, a follow-up study has been designed to investigate how low-frequency climate modes, such as the Pacific Decadal Oscillation, Interdecadal Pacific Oscillation, and Atlantic Multidecadal Oscillation, influence winter precipitation in this area.

Electronic supplementary material: Supplementary material is available in the online version of this article at https://doi.org/10.1007/s00376-024-4057-2.

REFERENCES

Ahmed, F., S. Adnan, and M. Latif, 2020: Impact of jet stream and associated mechanisms on winter precipitation in Pakistan. *Meteorol. Atmos. Phys.*, **132**(2), 225–238, https://doi.org/10.1007/s00703-019-00683-8.

Anders, A. M., G. H. Roe, B. Hallet, D. R. Montgomery, N. J. Finnegan, and J. Putkonen, 2006: Spatial patterns of precipitation and topography in the Himalaya. *Tectonics, Climate, and Landscape Evolution*, S. D. Willett, N. Hovius, M. T. Brandon, and D. M. Fisher, Eds., Geological Society of America, 39–53, https://doi.org/10.1130/2006.2398(03).

Barlow, M., M. Wheeler, B. Lyon, and H. Cullen, 2005: Modulation of daily precipitation over southwest Asia by the Madden–Julian oscillation. *Mon. Wea. Rev.*, **133**(12), 3579–3594, https://doi.org/10.1175/MWR3026.1.

Baudouin, J. P., M. Herzog, and C. A. Petrie, 2020a: Contribution of cross-barrier moisture transport to precipitation in the upper Indus River basin. *Mon. Wea. Rev.*, **148**(7), 2801–2818, https://doi.org/10.1175/MWR-D-19-0384.1.

Baudouin, J. P., M. Herzog, and C. A. Petrie, 2020b: Cross-validating precipitation datasets in the Indus River basin. *Hydrology and Earth System Sciences*, **24**(1), 427–450, https://doi.org/10.5194/hess-24-427-2020.

Baudouin, J. P., M. Herzog, and C. A. Petrie, 2021: Synoptic processes of winter precipitation in the Upper Indus Basin. *Weather and Climate Dynamics*, **2**(4), 1187–1207, https://doi.org/10.5194/wcd-2-1187-2021.

Bhattacharyya, S., S. Sreekesh, and A. King, 2022: Characteristics of extreme rainfall in different gridded datasets over India during 1983–2015. *Atmospheric Research*, **267**, 105930, https://doi.org/10.1016/j.atmosres.2021.105930.

Bolch, T., and Coauthors, 2012: The state and fate of Himalayan glaciers. *Science*, **336**(6079), 310–314, https://doi.org/10.1126/science.1215828.

Cannon, F., L. M. V. Carvalho, C. Jones, and B. Bookhagen, 2015: Multi-annual variations in winter westerly disturbance activity affecting the Himalaya. *Climate Dyn.*, **44**, 441–455, https://doi.org/10.1007/s00382-014-2248-8.

Cannon, F., L. M. V. Carvalho, C. Jones, and J. Norris, 2016: Winter westerly disturbance dynamics and precipitation in the western Himalaya and Karakoram: A wave-tracking approach. *Theor. Appl. Climatol.*, **125**, 27–44, https://doi.org/10.1007/s00704-015-1489-8.

Cannon, F., L. M. V. Carvalho, C. Jones, A. Hoell, J. Norris, G. N. Kiladis, and A. A. Tahir, 2017: The influence of tropical forcing on extreme winter precipitation in the western Himalaya. *Climate Dyn.*, **48**, 1213–1232, https://doi.org/10.1007/s00382-016-3137-0.

Chakraborty, A., and P. Singhai, 2021: Asymmetric response of the Indian summer monsoon to positive and negative phases of major tropical climate patterns. *Scientific Reports*, **11**(1), 22561, https://doi.org/10.1038/s41598-021-01758-6.

Chattopadhyay, J., 1970: Power spectrum analysis of atmospheric ozone content over north India. *Pure Appl. Geophys.*, **83**, 111–119, https://doi.org/10.1007/BF00875104.

Dahri, Z. H., E. Moors, F. Ludwig, S. Ahmad, A. Khan, I. Ali, and P. Kabat, 2018: Adjustment of measurement errors to reconcile precipitation distribution in the high-altitude Indus basin. *International Journal of Climatology*, **38**(10), 3842–3860, https://doi.org/10.1002/joc.5539.

Dahri, Z. H., and Coauthors, 2021: Spatio-temporal evaluation of gridded precipitation products for the high-altitude Indus basin. *International Journal of Climatology*, **41**(8), 4283–4306, https://doi.org/10.1002/joc.7073.

Dimri, A. P., 2006: Surface and upper air fields during extreme winter precipitation over the western Himalayas. *Pure Appl. Geophys.*, **163**, 1679–1698, https://doi.org/10.1007/s00024-006-0092-4.

Dimri, A. P., 2013: Interannual variability of Indian winter monsoon over the Western Himalayas. *Global and Planetary*

Change, **106**, 39–50, https://doi.org/10.1016/j.gloplacha. 2013.03.002.

Dimri, A. P., D. Niyogi, A. P. Barros, J. Ridley, U. C. Mohanty, T. Yasunari, and D. R. Sikka, 2015: Western disturbances: A review. *Rev. Geophys.*, **53**(2), 225–246, https://doi.org/10. 1002/2014RG000460.

Dimri, A. P., A. Chevuturi, D. Niyogi, R. J. Thayyen, K. Ray, S. N. Tripathi, A. K. Pandey, and U. C. Mohanty, 2017: Cloud-bursts in Indian Himalayas: A review. *Earth-Science Reviews*, **168**, 1–23, https://doi.org/10.1016/j.earscirev.2017. 03.006.

Hersbach, H., and Coauthors, 2020: The ERA5 global reanalysis. *Quart. J. Roy. Meteor. Soc.*, **146**(730), 1999–2049, https://doi.org/10.1002/qj.3803.

Hewitt, K., 2011: Glacier change, concentration, and elevation effects in the Karakoram Himalaya, Upper Indus Basin. *Mountain Research and Development*, **31**(3), 188–200, https://doi.org/10.1659/MRD-JOURNAL-D-11-00020.1.

Hoell, A., M. Barlow, and R. Saini, 2012: The leading pattern of intraseasonal and interannual Indian Ocean precipitation variability and its relationship with Asian circulation during the boreal cold season. *J. Climate*, **25**(21), 7509–7526, https://doi.org/10.1175/JCLI-D-11-00572.1.

Hoell, A., C. Funk, and M. Barlow, 2014: La Niña diversity and northwest Indian Ocean rim teleconnections. *Climate Dyn.*, **43**, 2707–2724, https://doi.org/10.1007/s00382-014-2083-y.

Hoell, A., M. Barlow, T. Y. Xu, and T. Zhang, 2018: Cold season southwest Asia precipitation sensitivity to El Niño–Southern Oscillation events. *J. Climate*, **31**(11), 4463–4482, https://doi.org/10.1175/JCLI-D-17-0456.1.

Hu, Y. Y., H. Huang, and C. Zhou, 2018: Widening and weakening of the Hadley circulation under global warming. *Science Bulletin*, **63**(10), 640–644, https://doi.org/10.1016/j.scib.2018. 04.020.

Huang, W. Y., T. P. Qiu, Z. F. Yang, D. Y. Lin, J. S. Wright, B. Wang, and X. S. He, 2018: On the formation mechanism for wintertime extreme precipitation events over the southeastern Tibetan Plateau. *J. Geophys. Res.: Atmos.*, **123**(22), 12 692–12 714, https://doi.org/10.1029/2018JD028921.

Hunt, K. M. R., and A. P. Dimri, 2021: Synoptic-scale precursors of landslides in the western Himalaya and Karakoram. *Science of the Total Environment*, **776**, 145895, https://doi.org/10. 1016/j.scitotenv.2021.145895.

Hunt, K. M. R., and S. N. Zaz, 2023: Linking the North Atlantic Oscillation to winter precipitation over the Western Himalaya through disturbances of the subtropical jet. *Climate Dyn.*, **60**(7–8), 2389–2403, https://doi.org/10.1007/s00382-022-06450-7.

Hunt, K. M. R., A. G. Turner, and L. C. Shaffrey, 2018a: The evolution, seasonality and impacts of western disturbances. *Quart. J. Roy. Meteor. Soc.*, **144**(710), 278–290, https://doi.org/10.1002/qj.3200.

Hunt, K. M. R., J. Curio, A. G. Turner, and R. Schiemann, 2018b: Subtropical westerly jet influence on occurrence of western disturbances and Tibetan Plateau vortices. *Geophys. Res. Lett.*, **45**(16), 8629–8636, https://doi.org/10.1029/2018 GL077734.

Jeelani, G., R. D. Deshpande, M. Galkowski, and K. Rozanski, 2018: Isotopic composition of daily precipitation along the southern foothills of the Himalayas: Impact of marine and continental sources of atmospheric moisture. *Atmospheric Chemistry and Physics*, **18**(12), 8789–8805, https://doi.org/10. 5194/acp-18-8789-2018.

Kamil, S., M. Almazroui, I. S. Kang, M. Hanif, F. Kucharski, M. A. Abid, and F. Saeed, 2019: Long-term ENSO relationship to precipitation and storm frequency over western Himalaya–Karakoram–Hindukush region during the winter season. *Climate Dyn.*, **53**, 5265–5278, https://doi.org/10. 1007/s00382-019-04859-1.

Kar, S. C., and S. Rana, 2014: Interannual variability of winter precipitation over northwest India and adjoining region: Impact of global forcings. *Theor. Appl. Climatol.*, **116**, 609–623, https://doi.org/10.1007/s00704-013-0968-z.

Lone, A. M., H. Achyuthan, S. Chakraborty, A. Metya, A. Datye, R. H. Kripalani, and A. A. Fousiya, 2020: Controls on the isotopic composition of daily precipitation characterized by dual moisture transport pathways at the monsoonal margin region of North-Western India. *J. Hydrol.*, **588**, 125106, https://doi.org/10.1016/j.jhydrol.2020.125106.

Midhuna, T. M., P. Kumar, and A. P. Dimri, 2020: A new Western Disturbance Index for the Indian winter monsoon. *Journal of Earth System Science*, **129**, 59, https://doi.org/10.1007/ s12040-019-1324-1.

Mohanty, U. C., O. P. Madan, P. L. S. Rao, and P. V. S., Raju, 1998: Meteorological fields associated with western disturbances in relation to glacier basins of western Himalayas during winter season. Center for Atmospheric Sciences, Indian Institute of Technology, New Delhi, Technical Report.

Nandargi, S., and O. N. Dhar, 2011: Extreme rainfall events over the Himalayas between 1871 and 2007. *Hydrological Sciences Journal*, **56**(6), 930–945, https://doi.org/10.1080/02626667. 2011.595373.

Nischal, R. Attada, , and K. M. Hunt, 2022: Evaluating winter precipitation over the western Himalayas in a high-resolution Indian regional reanalysis using multisource climate datasets. *Journal of Applied Meteorology and Climatology*, **61**(11), 1613–1633. https://doi.org/10.1175/JAMC-D-21-0172.1.

Orr, A., and Coauthors, 2022: Knowledge priorities on climate change and water in the Upper Indus Basin: A horizon scanning exercise to identify the top 100 research questions in social and natural sciences. *Earth's Future*, **10**(4), e2021EF002619, https://doi.org/10.1029/2021EF002619.

Pritchard, H. D., 2019: Asia's shrinking glaciers protect large populations from drought stress. *Nature*, **569**(7758), 649–654, https://doi.org/10.1038/s41586-019-1240-1.

Pritchard, H. D., D. Farinotti, and S. Colwell, 2021: Measuring changes in snowpack SWE continuously on a landscape scale using lake water pressure. *Journal of Hydrometeorology*, **22**(4), 795–811, https://doi.org/10.1175/JHM-D-20-0206.1.

Qiu, T. P., and Coauthors, 2019: Moisture sources for wintertime intense precipitation events over the three snowy subregions of the Tibetan Plateau. *J. Geophys. Res.: Atmos.*, **124**(23), 12 708–12 725, https://doi.org/10.1029/2019JD031110.

Ridley, J., A. Wiltshire, and C. Mathison, 2013: More frequent occurrence of westerly disturbances in Karakoram up to 2100. *Science of the Total Environment*, **468–469**, S31–S35, https://doi.org/10.1016/j.scitotenv.2013.03.074.

Schiemann, R., D. Lüthi, and C. Schär, 2009: Seasonality and interannual variability of the westerly jet in the Tibetan Plateau region. *J. Climate*, **22**(11), 2940–2957, https://doi.org/10. 1175/2008JCLI2625.1.

Singh, S. P., I. Bassignana-Khadka, B. Singh Karky, and E.

Sharma, 2011: *Climate change in the Hindu Kush-Himalayas: The state of current knowledge*. International Centre for Integrated Mountain Development (ICIMOD).

Singh, T., U. Saha, V. S. Prasad, and M. D. Gupta, 2021: Assessment of newly-developed high resolution reanalyses (IMDAA, NGFS and ERA5) against rainfall observations for Indian region. *Atmospheric Research*, **259**, 105679, https://doi.org/10.1016/j.atmosres.2021.105679.

Syed, F. S., F. Giorgi, J. S. Pal, and M. P. King, 2006: Effect of remote forcings on the winter precipitation of central southwest Asia. Part 1: Observations. *Theor. Appl. Climatol.*, **86**, 147–160, https://doi.org/10.1007/s00704-005-0217-1.

Tahir, A. A., P. Chevallier, Y. Arnaud, and B. Ahmad, 2011: Snow cover dynamics and hydrological regime of the Hunza River basin, Karakoram Range, Northern Pakistan. *Hydrology and Earth System Sciences*, **15**(7), 2275–2290, https://doi.org/10.5194/hess-15-2275-2011.

Thayyen, R. J., A. P. Dimri, P. Kumar, and G. Agnihotri, 2013: Study of cloudburst and flash floods around Leh, India, during August 4–6, 2010. *Natural Hazards*, **65**, 2175–2204, https://doi.org/10.1007/s11069-012-0464-2.

Yadav, R. K., K. R. Kumar, and M. Rajeevan, 2009: Increasing influence of ENSO and decreasing influence of AO/NAO in the recent decades over northwest India winter precipitation. *J. Geophys. Res.: Atmos.*, **114**(D12), D12112, https://doi.org/10.1029/2008JD011318.

Yadav, R. K., K. R. Kumar, and M. Rajeevan, 2010b: Climate change scenarios for Northwest India winter season. *Quaternary International*, **213**(1–2), 12–19, https://doi.org/10.1016/j.quaint.2008.09.012.

Yadav, R. K., J. H. Yoo, F. Kucharski, and M. A. Abid, 2010a: Why is ENSO influencing northwest India winter precipitation in recent decades?. *J. Climate*, **23**(8), 1979–1993, https://doi.org/10.1175/2009JCLI3202.1.

Yadav, R. K., D.A. Ramu, and A.P. Dimri, 2013 : On the relationship between ENSO patterns and winter precipitation over North and Central India. *Global and Planetary Change*, **107**, 50–58, https://doi.org/10.1016/j.gloplacha.2013.04.006.